ADVANCED MATERIALS
www.advmat.de

Efficient Deep-Blue Light-Emitting Diodes Through Decoupling of Colloidal Perovskite Quantum Dots

*Kyung Yeon Jang, Shin Young Hwang, Seung-Je Woo, Eojin Yoon, Chan-Yul Park, Seo Young Kim, Dong-Hyeok Kim, Hyeree Kim, Jinwoo Park, Edward H. Sargent, and Tae-Woo Lee**

Metal halide perovskite light-emitting diodes (PeLEDs) have exceptional color purity but designs that emit deep-blue color with high efficiency have not been fully achieved and become more difficult in the thin film of confined perovskite colloidal quantum dots (PeQDs) due to particle interaction. Here it is demonstrated that electronic coupling and energy transfer in PeQDs induce redshift in the emission by PeQD film, and consequently hinder deep-blue emission. To achieve deep-blue emission by avoiding electronic coupling and energy transfer, a QD-in-organic solid solution is introduced to physically separate the QDs in the film. This physical separation of QDs reduces the interaction between them yielding a blueshift of ≈7 nm in the emission spectrum. Moreover, using a hole-transporting organic molecule with a deep-lying highest occupied molecular orbital (≈6.0 eV) as the organic matrix, the formation of exciplex emission is suppressed. As a result, an unprecedently high maximum external quantum efficiency of 6.2% at 462 nm from QD-in-organic solid solution film in PeLEDs is achieved, which satisfies the deep-blue color coordinates of CIEy < 0.06. This work suggests an important material strategy to deepen blue emission without reducing the particle size to <≈4 nm.

1. Introduction

Metal halide colloidal perovskite nanocrystals (PeNCs) exhibit high color purity and tunability and also offer promising commercial feasibility due to their low-cost production, and highly scalable roll-to-roll process availability. Those properties provide their significant potential as light emitters for next-generation displays.[1–4] Meanwhile, a significant portion of perovskite light-emitting diode (PeLED) using PeNCs research has been engaged in enhancing the efficiency of PeLEDs without considering the required Commission Internationale de l'éclairage (CIE) color coordinates. However, to meet the requirements of next-generation displays, an increase in the efficiency of LEDs is not sufficient; they must also achieve suitable color coordinates for the three primary colors (i.e., red, green, and blue). Especially for the blue, deep-blue color with the CIEy < 0.06 is required to match the standard of ITU-R Recommendation BT.2100 (Rec. 2100).[5] Nevertheless, the method to obtain deep-blue emission (CIEy < 0.06) with high efficiency in colloidal PeNC-LEDs still lags behind. There are only a few reports of deep-blue colloidal PeNC-LEDs satisfying the stable CIEy < 0.06, which shows relatively limited efficiency of the maximum external quantum efficiency (EQE_{max}) of 4.4%.[6]

K. Y. Jang, S. Y. Hwang, S.-J. Woo, E. Yoon, C.-Y. Park, S. Y. Kim, D.-H. Kim, H. Kim, J. Park, T.-W. Lee
Department of Materials Science and Engineering
Seoul National University
1 Gwanak-ro, Gwanak-gu, Seoul 08826, Republic of Korea
E-mail: twlees@snu.ac.kr

E. H. Sargent
Department of Electrical and Computer Engineering
University of Toronto
35 St George Street, Toronto, ON M5S 1A4, Canada

The ORCID identification number(s) for the author(s) of this article can be found under https://doi.org/10.1002/adma.202404856

DOI: 10.1002/adma.202404856

E. H. Sargent
Department of Chemistry
Department of Electrical and Computer Engineering
Northwestern University
2145 Sheridan Rd, Evanston, IL 60208, USA

T.-W. Lee
Research Institute of Advanced Materials (RIAM)
Institute of Engineering Research
Soft Foundry
Interdisciplinary Program in Bioengineering
Seoul National University
1 Gwanak-ro, Gwanak-gu, Seoul 08826, Republic of Korea

T.-W. Lee
SN Display Co., Ltd.
1 Gwanak-ro, Gwanak-gu, Seoul 08826, Republic of Korea

Mixing of Br^- and Cl^- halide anions of perovskite (i.e., mixed halide perovskite) is a convenient way to tune the wavelength from green to blue.[7–9] However halide segregation in mixed-halide PeNCs is severe, and causes redshift in the emission spectrum during LED operation under an electric field, so this method has limited applicability to obtain a color-stable deep-blue spectrum.[10,11] A fundamental solution to obtain color-stable deep-blue emission can be exploiting the quantum confinement effect in colloidal perovskite quantum dots (PeQDs) by reducing the size of the PeQDs to below the exciton Bohr diameter.[12–14]

Accordingly, Br-only PeQDs with sizes ≈4 nm have been adopted due to their deep-blue emission ≈460 nm with high photoluminescence quantum yield (PLQY) > 90% in colloidal solution.[13] However, the emission spectrum redshifts in a film state for making devices, in that the electroluminescence (EL) spectrum of PeLEDs using such ≈4 nm sized PeQDs is typically limited to ≈470 nm (CIEy > ≈0.1) which is out of the deep-blue region. This discrepancy between the spectrum of PL and EL requires ultra-confined PeQDs in the particle size range of 2–3 nm to achieve the desired deep-blue EL emission.[15,16] However, PeQDs with a size below 4 nm require complex synthesis and purification methods because of secondary phases (e.g., 2D nanoplatelets, 0D Cs_4PbBr_6, etc.), and PeQDs get increasingly defective leading to low PLQY due to the high surface/volume ratio.[17] Therefore, exploiting the intrinsic deep-blue emission of ≈4 nm PeQDs without further reducing the size may be a feasible way to obtain deep blue PeLEDs that have high EQE.

Here we suggest a strategic material concept, a QD-in-solid solution to achieve deep-blue emission and be highly efficient at the same time. This material concept provides a solid film in which QDs are highly diluted. Hence, the terminology "solid solution" is used to refer to these highly diluted QDs dispersed in solid in our work. The QD-in-solid solution is designed to mitigate the spectral redshift observed in the film state, thereby utilizing the intrinsic deep-blue emission of ≈4 nm PeQDs while improving the PLQY. We have identified that the redshift of the EL spectrum is a result of the interactions between PeQDs in the film state, which are electronic coupling and energy transfer. As the strength of these interactions is reduced when the distance between PeQDs increases, spatial separation of PeQDs in solid solution effectively suppresses the electronic coupling and Förster resonance energy transfer (FRET), and thereby the deep-blue emission is successfully retained in film state. Because one major challenge in conventional approaches is that the simple dispersion of PeQDs in organic semiconductors often results in additional low-energy peaks due to the formation of excited complexes, our meticulous material design circumvents exciplex emission that degrades color purity and efficiency by incorporating hole-transporting organic molecules with suitable band alignment with PeQDs into the matrix. We used a hole-transporting organic material of N,N′-dicarbazolyl-3,5-benzene (mCP) which has the deep-lying highest occupied molecular orbital (HOMO) of ≈6.0 eV for a solid matrix, forming QD-mCP solid solution. This film of QD-mCP solid solution achieved the pure deep-blue EL emission with the CIE coordinates at (0.138, 0.058) and EQE_{max} of 6.2%. This result demonstrates that deep-blue EL emission (CIEy < 0.06) with high efficiency can be attained using ≈4 nm particles without needing to reduce the particle size.

2. Results and Discussion

2.1. QD-mCP Solid Solution for Deep-Blue Emission

$CsPbBr_3$ QDs of size ≈4 nm were used (properties: Supplementary texts 1–3 and Figures S1–S4, Supporting Information). They emitted an optimal deep-blue color (CIEy = 0.052) in their colloidal solution state. However, when these PeQDs alone were coated to form a film (QD-only film), the emission peak redshifted by ≈7 nm, to yield CIEy = 0.079, which is far from the reference deep-blue color (CIEy = 0.046). The shift is probably a result of electronic coupling and energy transfer (**Figure 1**A).

Electronic coupling can be explained as wavefunction tunneling to adjacent QDs. In the solution state, PeQDs are distant from each other in the solvent, therefore, effective quantum confinement without any electronic coupling enables deep-blue emission. Conversely, in the film state, an interspersed thin ligand layer (thickness < 2 nm) between PeQDs forms a shallow and finite barrier. The individual wavefunctions interact with the ones of adjacent QDs and thereby enable electronic coupling which causes a spectrum redshift by reducing the bandgap.[18]

Energy transfer can also contribute to the redshift. Due to the large overlap of the absorption and emission spectrum of PeQDs, FRET in the perovskite layer can induce a large amount of redshift. Furthermore, the size distribution induces bandgap divergence between PeQDs (Supplementary text 2, Supporting Information), so repeated energy transfer along the energy landscape of PeQDs eventually funnels to the PeQDs that have lower bandgaps, resulting in redshift of emission.

To solve this problem, PeQDs were separated by dispersing them in a solid organic matrix of mCP to form a QD-mCP solid solution (Figure 1B). The uniform distribution of QDs in the organic matrix film was confirmed by scanning electron microscopy (SEM) images (Figure S5, Supporting Information). Surprisingly, the PL emission remained deep blue with CIEy = 0.060, which is almost identical to the spectrum of the solution state (CIEy = 0.052) on the CIE 1931 diagram (Figure 1C,D). These results are due to suppressed electronic coupling and energy transfer in the film because the PeQDs are separated by a relatively long distance. To further elucidate the mechanism of this spectrum shift, the electronic coupling and energy transfer were analyzed quantitatively.

2.2. Quantitative Analysis of Electronic Coupling and Energy Transfer

We measured the PL peak wavelength λ_{PEAK} at various distances between PeQDs (QD–QD distances), controlled by tuning the ratio of PeQDs in the mCP matrix (**Figure 2**A). The QD–QD distance was calculated using the volumes of the perovskite core, of organic ligands, and of mCP (Supplementary text 4 and Figure S6, Supporting Information). The uniform dispersion of the QDs dispersed in mCP was confirmed by confocal PL microscopy (Figure S7) and atomic force microscopy (AFM) (Figure S8). Confocal PL microscopy reveals no micrometer-scale aggregation,

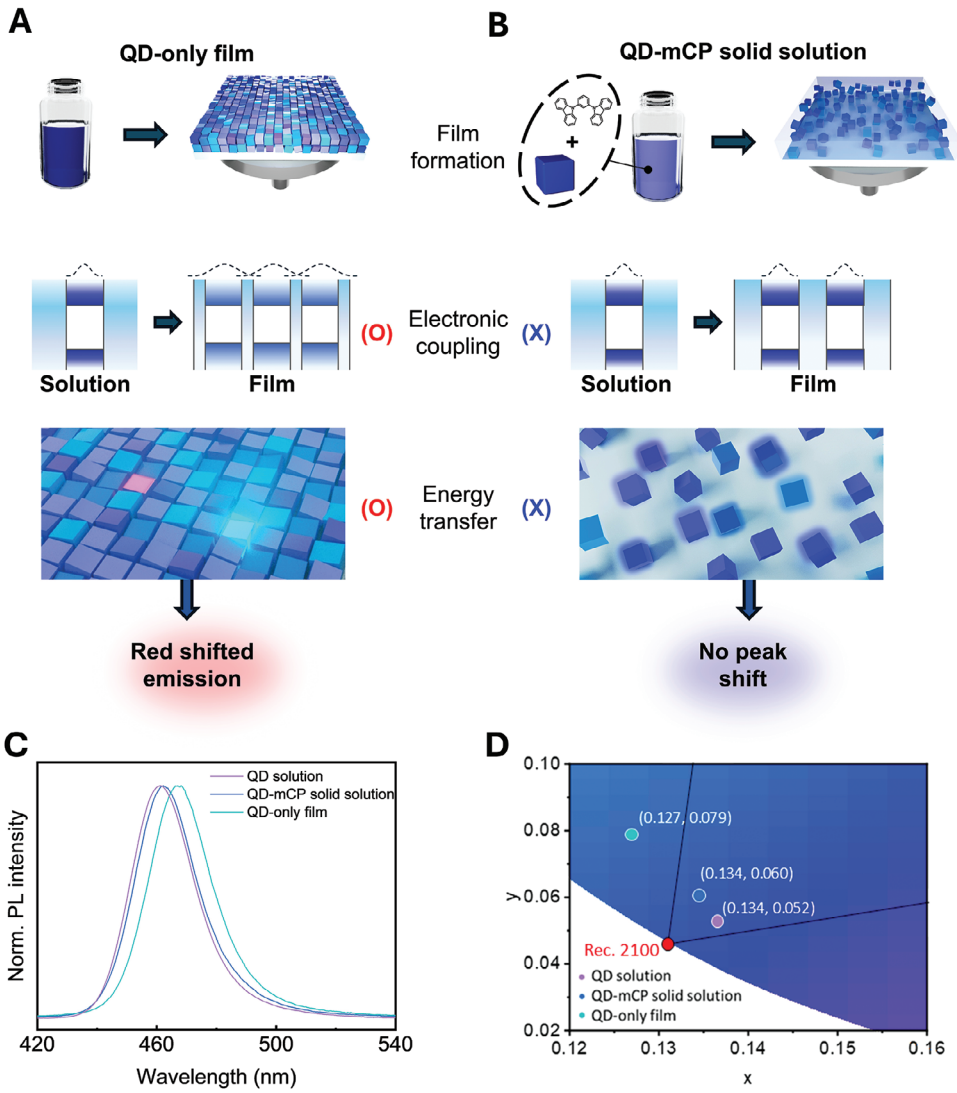

Figure 1. Retrieving deep-blue emission from QD-mCP solid solution. Scheme illustrating QD-QD interaction related to emission spectrum shifts in the A) QD-only film and B) QD-mCP solid solution. Closely packed QD-only film enables energy transfer and electronic coupling, whereas QD-mCP solid solution suppresses the energy transfer and electronic coupling by maintaining a distance between the QDs; as a result, the emission remained deep blue. C) Photoluminescence (PL) emission shift was observed in three samples of QD solution, QD-mCP solid solution, and QD-only film. D) Extended CIE 1931 diagram focused on the blue color. The red circle marks the standard deep-blue color coordinates (0.131, 0.046) suggested in Rec. 2100. Black solid lines connected to the red circle represent the boundary of the Rec. 2100 color gamut, linking to the standard green and red coordinates. Violet, blue, and sky-blue circles denote CIE coordinates derived from PL spectra of films. The coordinates of the QD-only film fall outside of the Rec. 2100 boundaries.

and the AFM image shows very smooth surfaces in the film of QD-mCP solid solution, with a root-mean-square roughness below 0.5 nm (Figure S8A–D). Phase images also demonstrated well-dispersed QDs in mCP (Figure S8E–H). Although there may be some local irregularities in the distribution of QDs, the overall average distance can be well estimated (Supplementary text 4), which is sufficient to observe different major interactions between QDs depending on the distance. QD–QD distance could not be increased beyond ≈11 nm due to damage to PeQDs upon dilution, likely caused by ligand detachment in highly diluted conditions. λ_{PEAK} decreased as the QD–QD distance increased, as expected. Additionally, λ_{PEAK} decreased rapidly in two stages (**Stage I** in the range of 1.8-3.8 nm and **Stage II** in the range of 3.8–11.3 nm); the presence of these stages indicates the presence of different major interactions (electronic coupling and energy transfer) between PeQDs depending on the distance. To elucidate the distinct behavior of PL wavelength shift, we selected three representative films at points **a**, **b**, **c** corresponding to the boundaries of the stages. These include point **a**; QD-only film (QD 100 wt%), point **b**; QD-mCP solid solution at the transition point (QD 60 wt.%), and point **c**; highly diluted QD-mCP solid solution (QD 10 wt%). Their normalized PL spectra are presented in Figure 2B. Additionally, the film at a point **b′**, selected between points **b** and **c**, was further investigated to illustrate the intermediate stage of the energy transfer suppression, as detailed in Supplementary text 5 and Figure S9.

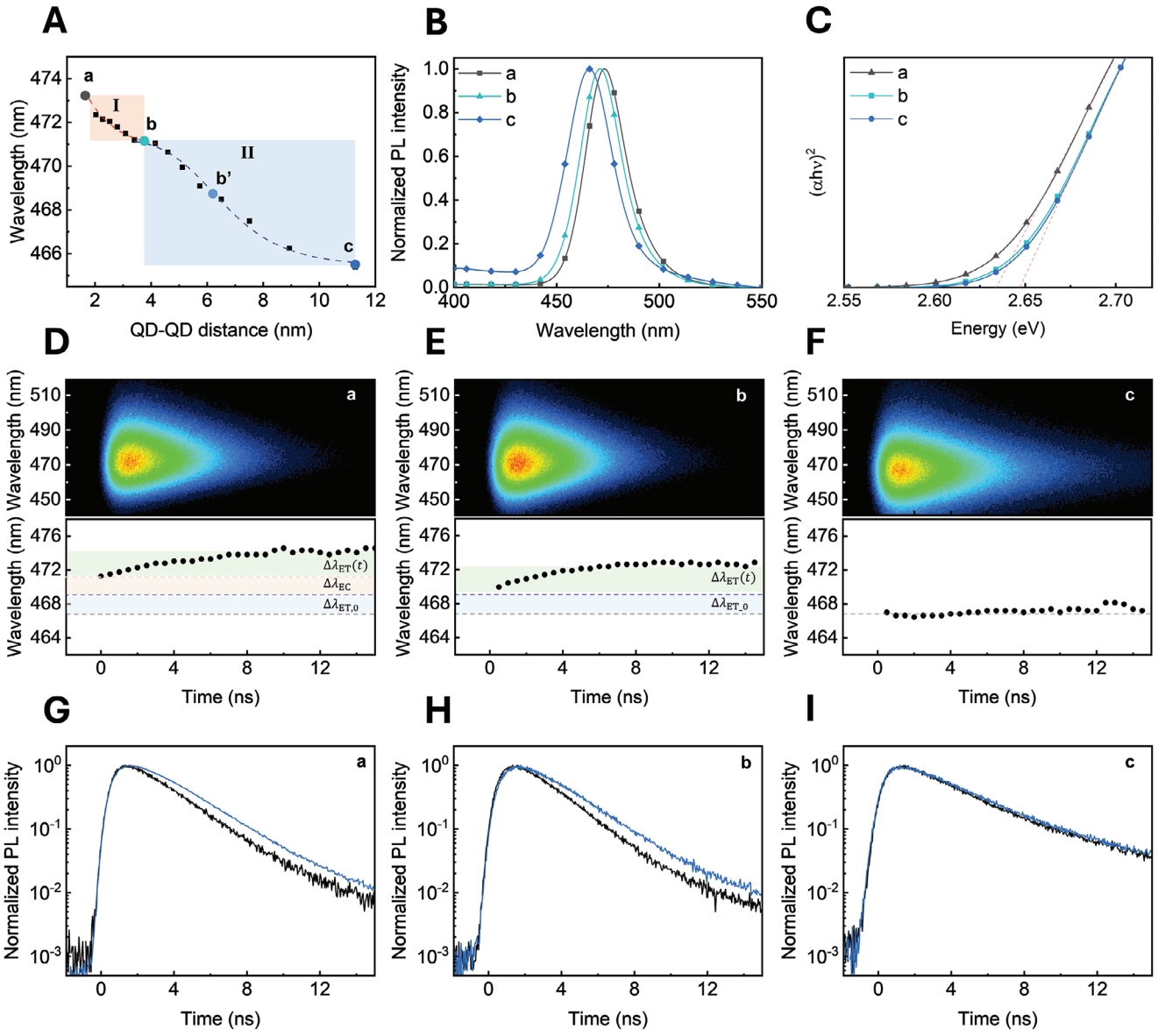

Figure 2. PL characteristics depend on the interactions between PeQDs in the film. A) The PL peak wavelength of PeQD-mCP film depends on QD–QD distance. The wavelength change is divided into two stages: electronic coupling dominant stage I (red square), and energy transfer dominant stage II (blue square). Red and blue dashed lines are the fitted curves based on the strength of electronic coupling, and energy transfer efficiency depending on the QD–QD distance, respectively. Three representative films at points a, b, and c are depicted as filled circles at the boundary of each stage. Point b′, selected as the intermediate point of the energy transfer. (detailed data in Supplementary text 5 and Figure S9) B) Normalized PL spectrum and C) Tauc plot of representative films at points a, b, and c. Streak camera images (top) and extracted peak wavelengths at 500-ps intervals (bottom) of D) film at point a, E) film at point b, F) film at point c. The peak wavelength shift is divided into three component areas (red: peak shift by electronic coupling $\Delta\lambda_{EC}$; green: time-dependent peak shift by energy transfer $\Delta\lambda_{ET,t}$; blue: constant peak shift by energy transfer). PL lifetime where grey line shows shorter wavelength side and blue line shows long wavelength side relative to the spectrum center, for G) film at point a, H) film at point b, and I) film at point c, obtained from the streak camera image.

In stage **I**, electronic coupling was anticipated to occur within the vicinity of a few nanometers.[19] We calculated the optical bandgap $E_{g,\,opt.}$ of PeQD films by using the Tauc plot (Figure 2C) obtained using UV–vis spectroscopy (Figure S10). Although all films were fabricated using the same PeQDs, $E_{g,\,opt.}$ in the film at point **a** shifted toward lower $E_{g,\,opt.}$ = 2.634 eV, whereas the films at points **b** and **c** showed identical curves that had $E_{g,\,opt.}$ = 2.647 eV. This difference in $E_{g,\,opt.}$ confirms the existence of electronic coupling in the film at point **a** within the closely packed QDs film.[19]

The wavelength difference $\Delta\lambda \approx 2.3$ nm, derived from the $E_{g,\,opt.}$ that was obtained from the Tauc plots of the films at points **a** and **b**, aligns well with the change $\Delta\lambda \approx 2.1$ nm at stage **I** (Figure 2A,C). Thus, we infer that the $\Delta\lambda$ observed in stage **I** arises primarily from the electronic coupling effect which we defined as $\Delta\lambda_{EC}$. Furthermore, the PL shift in stage **I** can be fitted

well using an exponential function, and therefore shows the same tendency as electronic coupling, which decays exponentially as QD–QD distance increases (Supplementary text 6, Supporting Information).[20,21]

In stage **II**, the energy-transfer mechanism is expected to be the main reason for emission redshift because this mechanism occurs over a longer distance than electronic coupling. Energy transfer occurs over time, so we used a streak camera to measure the time-dependent PL spectrum (Figure 2D–F). λ_{PEAK} was collected in 500-ps intervals. The films at points **a** and **b** exhibit a dynamic ≈3 nm redshift (which we define as $\Delta\lambda_{ET,t}$) over time. This trend is evidence of repeated energy transfer (Figure 2D,E) along with the energetic disorder of PeQDs.[22,23] In the film at point **c**, λ_{PEAK} was constant, which indicates that energy transfer is suppressed as a result of the sufficiently long distance between QDs. After excluding $\Delta\lambda_{EC}$ and $\Delta\lambda_{ET,t}$, an additional constant gap $\Delta\lambda_{ET,0}$ was observed in the films at points **a** and **b** (Figure 2D,E), but not in the film at point **c** (Figure 2F). This phenomenon may be a result of energy transfer within an extremely short time (~picoseconds) after excitation, which cannot be observed in the current optical setup.[24]

The PL-decay lifetimes of the films at points **a** and **b** were longer at wavelengths > λ_{PEAK} than at wavelengths < λ_{PEAK} (Figure 2G,H). These results suggest that the initial deep-blue emission from small QDs transfers energy toward large QDs, so the spectrum is redshifted, and emission is delayed. In contrast, the PL lifetimes of the film at point **c** were identical at wavelengths on both sides of λ_{PEAK}; this result indicates that energy transfer was effectively prevented in this film (Figure 2I). PL spectra derived from the prompt-time range (0 to 2 ns) and the delayed-time range (10 to 20 ns) also directly show that the energy transfer induced redshift in the PL emission in the film points at **a** and **b** (Figure S11).

Wavelength change induced by energy transfer in stage **II** can be fitted by a modified FRET efficiency equation[25] with the assumption that FRET efficiency when multiplied by a constant C, can account for the wavelength change,

$$\lambda_{ET}(d) = \Delta\lambda_{ET}(d) + \lambda_0 = C\frac{R_0^6}{R_0^6 + d^6} + \lambda_0 \quad (1)$$

where $\lambda_{ET}(d)$ is the peak wavelength observed in stage **II**, $\Delta\lambda_{ET}(d)$ is wavelength shift induced by energy transfer at the QD–QD distance of d, λ_0 is wavelength without energy transfer, R_0 is Förster radius, R is QD–QD distance, and C is a constant that converts FRET efficiency to wavelength. Although the direct relationship between FRET efficiency and emission wavelength is complicated, stage **II** is well-fitted by Equation 1, which yields $R_0 = 6.56\pm 0.17$ nm. This value is similar to $R_0 = 5.75$ nm which is calculated from the overlap of absorption and emission spectra (Supplementary texts 6-7 and Figure S12, Supporting Information). Finally, the total redshift $\Delta\lambda_{Tot}$ of the blue PeQD film can be described as

$$\Delta\lambda_{Tot} = \Delta\lambda_{EC} + \Delta\lambda_{ET} = \Delta\lambda_{EC} + (\Delta\lambda_{ET,t} + \Delta\lambda_{ET,0}) \quad (2)$$

where $\Delta\lambda_{EC}$ = 2.1 nm (11.7 meV) and $\Delta\lambda_{ET}$ = 5.7 nm (32.2 meV) in our system. This result indicates that energy transfer has about twice as much effect as electronic coupling on the redshift in our PeQD film.

It should be noted that the degree of electronic coupling and energy transfer can be further modified depending on the ligand length, QD size or size distribution of PeQD. For example, in our QDs, the interparticle distance in the QD-only film is 1.8 nm, which is due to the presence of organic ligands. Replacing these organic ligands with inorganic NaBr ligands can reduce the interparticle distance to 0.7 nm, resulting in a significant peak redshift of 74 meV, primarily driven by electronic coupling.[26] Regarding QD size, using extremely small 1.8 nm-InP QDs, a large peak redshift of 140 meV was observed, attributed to the more pronounced electronic coupling due to the smaller QD size.[27] Conversely, maintaining a narrow size distribution of the QDs can mitigate the redshift caused by energy transfer.[24,28]

In summary, using smaller QDs, reducing the interparticle distance, and having a wide size distribution can strengthen the effects of electronic coupling and energy transfer. Therefore, minimizing QD–QD interactions by controlling these factors is essential to prevent the redshift of emission. Similarly, the PL of films that use green-emitting $CsPbBr_3$ nanocrystals undergo negligible peak shift, because the weak confinement region has size-independent emission, and because the effect of electronic coupling is insignificant in large nanocrystals (Figure S13).

2.3. Fabrication and EL Characteristics of PeLEDs

We used the QD-mCP solid solution as the emissive layer (EML) of PeLEDs to achieve deep-blue emission. Utilization of the QD-mCP solid solution requires additional considerations, particularly regarding solvent orthogonality and exciplex formation. Hole-transporting polymers such as poly(N,N"-bis-4-butylphenyl-N,N"-bisphenyl)benzidine (poly-TPD) or poly(9-vinylcarbazole) (PVK) are commonly used as the hole-transport layer (HTL) for PeLEDs when octane is used as the solvent used for nanocrystals. However, the solvent used for QD-mCP solid solution is toluene, and these HTLs have poor solvent resistivity against it, so the HTL polymer becomes partially solvated and intermixes within the EML. These processes lead to undesirable emission by the HTL itself, or exciplex emission when it contacts the electron-transport layer (ETL) (Figure S15).

To avoid this problem, we fabricated a cross-linkable HTL by using 3,5-di-9H-carbazol-9-yl-N,N-bis[4-[[6-[(3-ethyl-3-oxetanyl)methoxy]hexyl]oxy]phenyl]benzenamine (Oxe-DCDPA) on poly(3,4-ethylenedioxythiophene) polystyrene sulfonate (PEDOT:PSS).[29] A crosslinking reaction between the oxane group in Oxe-DCDPA and PEDOT:PSS enables perfect solvent resistivity during deposition of that EML, and thereby prevents the formation of exciplexes.

For the organic matrix for the PeQD solid solution, we also tested other small molecules (tris(4-carbazoyl-9-ylphenyl)amine (TCTA) and 2,2′,2″;-(1,3,5-Benzinetriyl)-tris(1-phenyl-1-H-benzimidazole) (TPBi), but they yielded interfacial exciplex emission and poor efficiency (Figure S16), compared to the high efficiency and clear QD emission when mCP was used.

The final device structure was indium tin oxide (ITO)/PEDOT:PSS (30 nm)/Oxe-DCDPA (15 nm)/EML/3′,3‴,3⁗-(1,3,5-triazine-2,4,6-triyl) tris([1,1′-biphenyl]−3-carbonitrile))

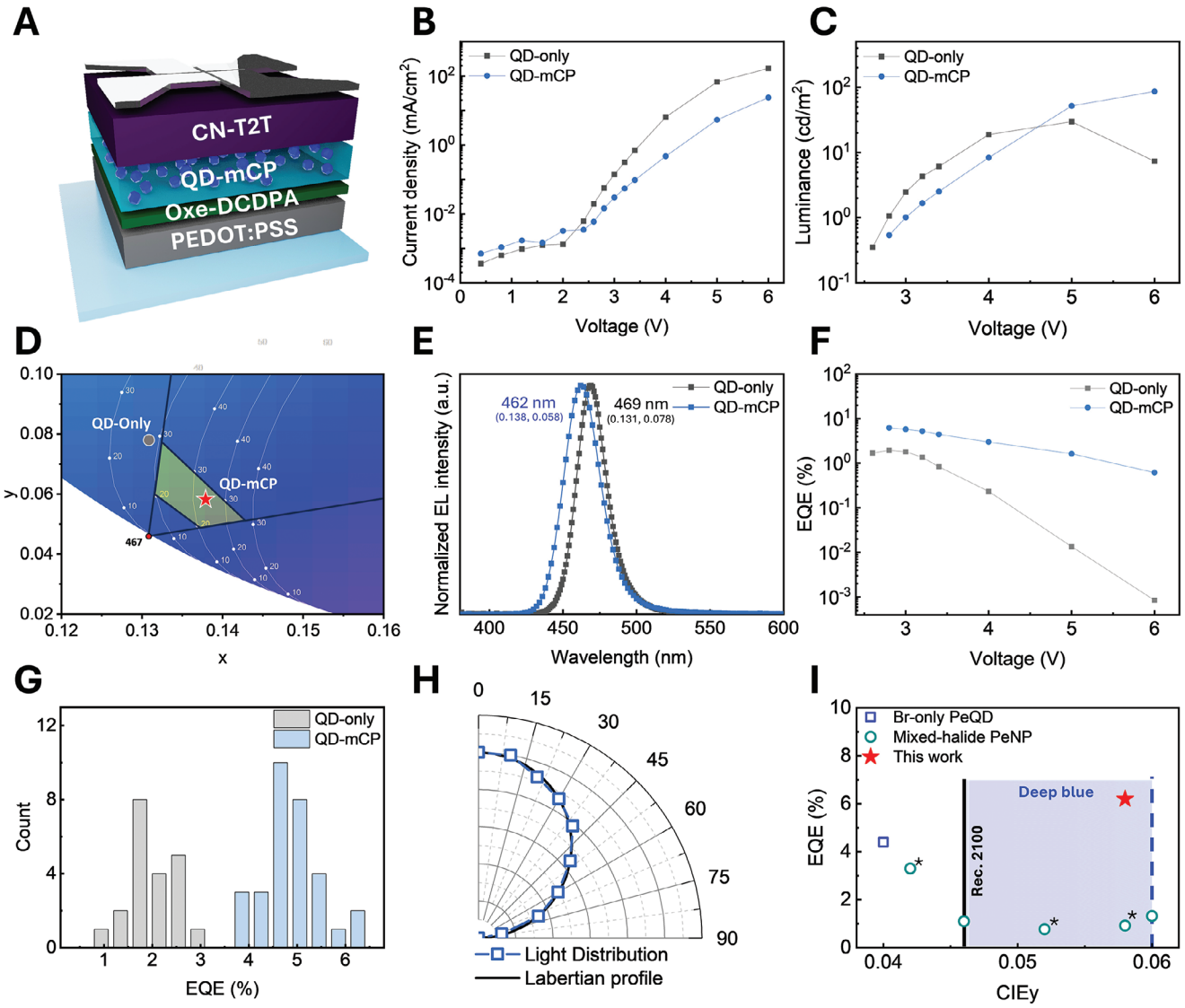

Figure 3. EL characteristics of PeLEDs. A) Device structure of PeLEDs B) Current density-voltage curve, C) Luminance-voltage curve of PeLEDs, D) CIE coordinates of QD-only (black circle) and QD-mCP solid solution (red star) PeLEDs in the magnified CIE 1931 diagram. Black solid line: Rec. 2020 color standard. E) Normalized EL spectrum of PeLEDs (more detailed measurements at 0.2 V steps are shown in Figure S14, in the Supporting Information), F) external quantum efficiency (EQE)-voltage curve of PeLEDs, G) histogram EQE of PeLEDs, H) angle-dependent EL intensity, I) EQE chart of deep-blue PeLEDs using colloidal perovskite quantum dots or nanoparticles (star: present result; filled: EQE obtained considering the full angular EL distribution; hollow: EQE calculated using the Lambertian assumption; *: CIEy calculated from digitized data).

(CN-T2T) (45 nm)/LiF (1 nm)/Al (100 nm) (**Figure 3A**). QD-mCP solid solution PeLEDs exhibited lower current density J than QD-only PeLEDs; the difference can be attributed to the lower carrier mobility in mCP than in the PeQDs (Figure 3B). However, the QD-mCP solid solution showed higher luminance than QD-only PeLEDs at the same J; this difference indicates that radiative recombination was more efficient in the QD-mCP solid solution than in the QD-only emissive layer (Figure 3C).

As QD-mCP solid solution retained deep-blue PL emission even in the film state (Figure 2B), PeLEDs that use QD-mCP solid solution also had a deep-blue EL spectrum that had λ_{PEAK} = 462 nm, with CIE color coordinates (0.138, 0.058) that meet the standard of Rec. 2100. However, PeLEDs that used only QDs had redshifted λ_{PEAK} = 469 nm and CIE color coordinates (0.131, 0.078) which do not satisfy the Rec. 2100 color gamut (Figure 3D,E). Thus, the QD-mCP solid solution can achieve the ideal blue-emission for display applications. Meanwhile, the EL spectrum of the QD-mCP solid solution-based PeLED showed a wider full width at half maximum (FWHM) of ≈29 nm, whereas QD-only PeLED exhibited a narrower FWHM of ≈24 nm. The wider FWHM in the QD-mCP solid solution device is attributed to inhomogeneous line broadening induced by the size distribution of QD ensembles (Figure S17A).[30,31] Conversely, the narrower FWHM in the QD-only PeLED can be explained as the result of energy transfer, which narrows the "effective size

distribution" of QDs that actually contribute to the emissions (Figure S17B).

QD-mCP solid solution-based PeLEDs had higher EQE_{max} = 6.20% than PeLEDs that use QD-only film, which had EQE_{max} = 1.95% (Figure 3F,G). The EQE calculation was supported by the full angular EL distribution (Figure 3H). This improvement can be attributed to an increase in the balance of charge injection. Regarding band alignment, PeQDs have a deep valence band maximum of −6.2 eV and a shallow conduction band minimum (CBM) of -3.5 eV, measured by UV photoelectron spectroscopy (UPS) and $E_{g,\,opt.}$ (Figure S18). Meanwhile, a HOMO level of −5.8 eV of Oxe-DCDPA, and a LUMO level of −2.8 eV of CN-T2T leads to the high energy offset of hole injection but no barrier in electron injection, therefore excess electron injection into EML was expected. Furthermore, there exists a significant difference in mobility between HTL and ETL, where Oxe-DCDPA has low hole mobility $\mu_h \approx 10^{-7}$ cm^2 V^{-1} s^{-1} whereas CN-T2T has high electron mobility $\mu_e \approx 10^{-5}$–10^{-4} cm^2 V^{-1} s^{-1}.[29,32] The combination induces electron-dominant, unbalanced charge injection. In contrast, mCP has high $\mu_h = 1.2 \times 10^{-4}$ cm^2 V^{-1} s^{-1} and low $\mu_e = 4 \times 10^{-5}$ cm^2 V^{-1} s^{-1},[33] and deep HOMO level of −6.0 eV facilitates hole injection by reducing the energy offset, whereas its high LUMO level of −2.4 eV retards electron injection. Thereby mCP helps to achieve balanced charge injection.[34] The energy diagram of the QD-mCP-based PeLED is shown in Figure S19 to help the understanding.

Additionally, to clarify the reason for the increment of EQE in the QD-mCP device, we investigate the interfacial exciton quenching between the EML and HTL. PL lifetime was measured using time-correlated single-photon counting (TCSPC), for the QD-only or QD-mCP film on the glass substrate with and without ITO/PEDOT:PSS/Oxe-DCDPA layer (Figure S20A, B). For the QD-only film, there was a significantly shortened PL lifetime, along with a decreased PL intensity (Figure S20 A, C), indicating the existence of a non-radiative recombination path at the interface. Meanwhile, for the QD-mCP film, there was negligible change in PL lifetime and PL intensity (Figure S20B, D), indicating that suppressed interfacial exciton quenching on the HTL when using QD-mCP film.

We also considered the outcoupling efficiency. In PeLEDs, the morphology of the EML can enhance the light outcoupling efficiency by suppressing the lateral waveguide mode through scattering, particularly when having discrete sub-micrometer grains.[35,36] However, based on our AFM image of the QD-mCP solid solution, which shows a very smooth surface without QD aggregations, the increased light outcoupling by scattering would be negligible (Figure S8C).

The outcoupling efficiency of thin film LED devices is highly affected by the refractive indices of the layers comprising the device. Therefore, we performed optical simulations of the QD-only and QD-mCP devices. Here, the refractive indices of QD-only and QD-mCP EML were determined by analyzing the variable angle ellipsometric spectroscopy (VASE) measurements. The refractive indices of QD-only and QD-mCP EML were determined to be quite low for n ≈ 1.74 at 460 nm for QD-only film, and a slightly higher n ≈ 1.76 at 460 nm for QD-mCP film (Figure S21A, B). We attribute the low refractive index of $CsPbBr_3$ QDs to the smaller perovskite core size and the relatively large amount of organic ligand due to the high surface-to-volume ratio. The slightly higher refractive index of the QD-mCP film is due to the higher refractive index of mCP (n ≈ 1.77 at 460 nm) compared to the QDs. As a result, the higher refractive index of EML in QD-mCP-based PeLED leads to a higher waveguide loss of 7.0%, compared to 5.5% for the QD-only based PeLED, which originates from the total internal reflection at the Oxe-DCDPA (n ≈ 1.67 at 460 nm) and EML interface.

The refractive index can also affect the effective thickness of the layer in the LED device. Based on the simulation results, an ETL thickness ≈60 nm is optimal for maximum outcoupling efficiency ($EQE_{Sim,max}$) whereas we used an ETL of 45 nm which was ideal for the fabricated device, probably due to the combined electrical- and optical- effects. Since the QD-mCP film has a higher refractive index than the QD-only film, the QD-mCP device exhibits a higher effective EML thickness. Therefore, the higher refractive index of the QD-mCP film suggests that QD-mCP devices have a more favorable optical path length compared to QD-only devices. Consequently, the shorter optimized ETL thickness for $EQE_{Sim,max}$ of 59 nm was determined for the QD-mCP devices, compared to 62 nm for the QD-only device. Meanwhile the value of $EQE_{Sim,max}$ is almost similar between the two devices (QD-only: $EQE_{Sim,max}$ = 22.3%, QD-mCP: $EQE_{Sim,max}$ = 22.1%).

Combining these optical effects result in simulated EQE (EQE_{sim}) values of 17.9%, and 18.9% for QD-only and QD-mCP devices, respectively (Figure S21C, D). However, compared to the more than two fold increase in EQE in the QD-mCP device, the efficiency increment due to light outcoupling is negligible. Therefore, charge balance and suppressed interfacial exciton quenching are likely the major factors for the higher EQE in the QD-mCP device.

2.4. EL Recombination Mechanism of QD-mCP-Based PeLEDs

When mCP acts as the host and PeQD serves as the dopant, two recombination mechanisms may operate within the system. One is trap-assisted recombination by direct charge carrier trapping into PeQDs. The other mechanism is Langevin recombination, which involves Förster or Dexter energy transfer from mCP to PeQDs after exciton formation in mCP. During this process, due to the presence of a 1-2 nm thick ligand layer surrounding PeQDs, Dexter energy transfer between PeQD and mCP is expected to be negligible. Based on the following analysis, we anticipate that Langevin recombination will serve as the predominant recombination process.

We first evaluated the efficiency of energy transfer between mCP and PeQDs. For energy transfer to be efficient, the emission of the host must overlap with the absorption of the dopant. Importantly, the emission spectrum of mCP overlaps substantially with the absorption spectrum of QDs; this observation suggests that mCP can be an appropriate host material of the PeQD solid solution for LED devices (**Figure** 4A).

Energy transfer from mCP to PeQDs was confirmed using PL-lifetime measurements at emission wavelengths of 400 nm (emission of mCP) and 462 nm (emission of PeQDs) for QD-only film, mCP-only film, and QD-mCP solid solution, (Figure 4B,C). TCSPC was conducted at an excitation wavelength of 266 nm, then each curve was fitted using a tri-exponential decay function.

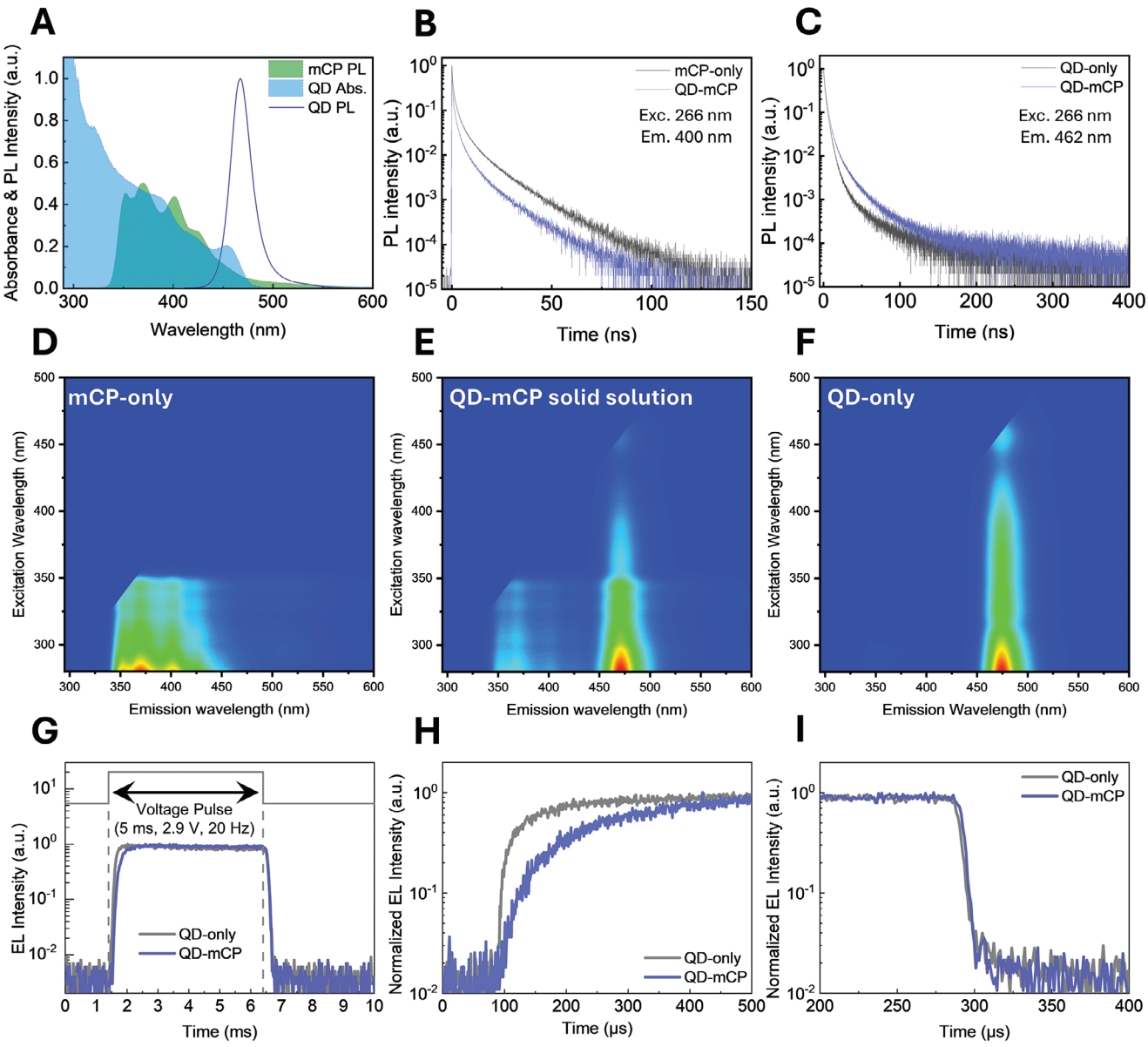

Figure 4. Recombination mechanism in QD-mCP solid solution PeLEDs. A) PL and absorption spectrum of PeQDs and mCP. PL lifetime of B) mCP and C) PeQDs in solid solution, compared to single-type film. Emission/excitation 2D mapping of D) mCP-only film, E) QD-mCP solid solution, and F) QD-only film. G) Full TrEL signal in the timescale of 10 ms, magnified TrEL signal in H) rise region, and I) decay region.

In comparison to the single type-film (QD-only or mCP-only film) and the QD-mCP solid solution, the average PL lifetime of mCP-only film decreased from 6.22 ns to 4.70 ns, whereas that of PeQDs increased from 3.96 to 6.00 ns; these results indicate energy transfer from mCP to PeQDs (Table S5).

Emission/excitation 2D mapping was conducted for mCP-only film, QD-mCP solid solution, and QD-only film (Figure 4D,F). In the presence of mCP, the PL intensity of PeQDs increased significantly in the excitation wavelength region of 280–360 nm. At this region, mCP absorbs the excitation light and transfers it to the PeQDs. However, at excitation wavelengths > 360 nm, the PL intensity of PeQDs decreased due to the absence of energy transfer from mCP. These results further support the existence of an efficient energy-transfer process between mCP and PeQDs.

To see the effect of trap-assisted recombination, the time-resolved electroluminescence (TrEL) was measured in PeLEDs that had different EMLs of QD-only, and QD-mCP. A 5-ms width pulse with a frequency of 20 Hz was applied at 2.9 V (Figure 4G). If charge carrier trapping occurs, PeQDs electrons would be deeply trapped in the PeQDs because of the large energy differences of CBM and LUMO levels between PeQDs (−3.5 eV) and mCP (−2.4 eV). Meanwhile, relatively mobile hole hopping along the mCP would allow the recombination of holes with pre-trapped electrons in PeQDs.

The rise time in PeLEDs that use QD-mCP was significantly slower than in PeLEDs that use only QDs. The difference indicates that charge carriers are more likely injected through the mCP and then transferred to QDs either by energy transfer or charge carrier trapping, rather than being directly injected into QDs (Figure 4H). During the decay of TrEL, after the external field is turned off, recombination of long-lived trapped charges in organic solids is often considered to be result of spike, overshoot or long-lived decay.[37] However, the PeLED that used QD-mCP solid solution did not show notable spike or overshoot (Figure 4I). Although trap-assisted recombination exists as an emission path can usually lead an overshoot or spike in the decay, if the device has no counterpart charge-blocking layer and only a single-type charge carriers are trapped, an overshoot or spike in the decay cannot appear.[38] However, the QD-mCP solid solution is well confined between Oxe-DCDPA and CN-T2T, which have ideal LUMO and HOMO levels to act as electron-blocking and hole-blocking layers, respectively. Therefore, in the QD-mCP solid solution, Langevin recombination would be the dominant recombination mechanism, rather than trap-assisted recombination.

The impact of the Langevin recombination mechanism on the performance of the QD-mCP solid solution device was examined by analyzing the degradation of QDs caused by injected charges within the LED device (Figure S22A). The PL intensity of the emissive layer was measured under operational conditions. Emissions were collected four times for 15 s at each voltage step, with the voltage inceased by 0.2 V each time (Figure S22A).

A reduction in the PL intensity of the QDs was observed starting at 2.4–2.6 V, corresponding to the onset of the current increase in the *J*–*V* curve. The PL intensity continued to decrease with increasing voltage, showing an ≈95% reduction at 4.0 V in the QD-only device. This degradation is irreversible, as the PL intensity did not recover after removing the voltage. Conversely, the QD-mCP solid solution device showed less PL intensity decrease, maintaining ≈50% PL intensity at 4.0 V (Figure S22A).

This result indicates permanent damage to the QDs by injected charges, and the QD-mCP solid solution structure can prevent this degradation. A similar result has been reported using CdSe/CdS red chalcogenide QDs, attributed to the reduction reaction of Cd^{2+} into Cd^{0}.[39] While there is still no in-depth exploration of charge-induced degradation in perovskite QDs, redox reaction dynamics induced by e-beam, which initiate the reduction of Pb^{2+} into Pb^{0} and the oxidation of $2Br^{-}$ into Br_2, have been reported to be a degradation path of $CsPbBr_3$ nanoparticles.[40]

The degradation of QDs can be mitigated in QD-mCP devices because mCP modulates charge injection. Langevin recombination allows charge carriers to form excitons in mCP, which are then transferred to the QDs, preventing excessive or unbalanced charge injection. Typically, QDs encountered excessive electron injection due to their low electron injection barrier and high hole injection barrier. In such cases, the unbalanced majority carrier (electron) remains in the emissive layer, thus inducing redox reactions more readily. However, through the energy transfer process, mCP suppresses direct electron injection and instead transfers exciton (electron–hole pairs). Therefore, the redox reaction induced by these carriers can be mitigated.

In summary, the energy transfer process is proposed to protect QDs from degradation by injected charges, enhancing device efficiency and stability. The time-dependent relative PL intensity was measured at a constant voltage of 3.0 V, where the EQE_{max} is achieved. QD-mCP devices showed only a 10% drop after 20 min, while QD-only devices exhibited a 20% drop (Figure S22B). The EL device stability was obtained at an initial luminance of $L_0 = 10$ cd m^{-2} applying a constant current and measuring the relative luminance. The QD-mCP device demonstrated a longer half-lifetime (T_{50}) of 201 s compared to the QD-only device ($T_{50} = 68$ s) (Figure S22C). Although the overall device stability is currently limited, the primary instability arises from severe QD degradation due to charge injection, and the QD-mCP structure can mitigate this instability through the energy transfer process. More intense exploration and development are still required to improving device stability.

3. Conclusion

Quantum-confined PeQDs are promising blue emitters for the PeLEDs, but when these PeLEDs are deposited as a film, the emission peak shifts toward red, and this change hinders the achievement of deep blue emission (CIE y < 0.6). Both electronic coupling and energy transfer are responsible for the redshift, and the short distance between QDs and size-dependent emission of PeQDs exacerbate those effects. Considering the wavelength redshift in the film state, energy transfer contributes about twice as strongly to the redshift as electronic coupling does. To suppress this redshift, we developed a method to disperse PeQDs uniformly in a solid solution, by using the hole-transporting organic molecule mCP as a matrix, which maintains a distance between PeQDs. The QD-mCP solid solution structure suppresses the electronic coupling, so maintains a bandgap identical to that of the QD liquid solution. Time-resolved spectroscopy confirmed that energy transfer was suppressed in the QD-mCP film. PeLEDs that used QD-mCP film as an emitting layer emitted deep blue with CIE coordinates of (0.138, 0.058). This work can help to achieve deep-blue emission in the PeLEDs by using PeQDs without further reducing the particle size and can provide insights to guide the design of deep blue PeQD films and control the photophysical properties for PeQD emitters that have a well-defined emission color for display applications.

4. Experimental Section

Materials: Cs_2CO_3 (99%, Sigma–Aldrich), $PbBr_2$ (98%, Sigma–Aldrich) Oleylamine (70%, Sigma–Aldrich), Oleic acid (90%, Sigma–Aldrich), Hydrobromic acid (48 wt% in H_2O, Sigma–Aldrich), 1-octadecene (90%, Sigma–Aldrich), $ZnBr_2$ (98%, Tokyo Chemical Industry), methyl acetate (99.5%, Samchun Chemicals), Hexane (96%, Samchun Chemicals), Toluene (99.8% anhydrous, Sigma–Aldrich), Benzoyl bromide (98%, Tokyo Chemical Industry), PEDOT:PSS (Clevios PVP AI 4083), and LiF (99.99%, Sigma–Aldrich) were used directly as received.

Synthesis and Purification of PeQDs: Cs_2CO_3 (325.8 mg, 1 mmol, containing 2 mmol Cs) and OA (0.7 mL) were loaded into a 100-mL 3-neck flask along with 9 mL of octadecene, then dried at 120 °C until the gas evolution stopped. At room temperature, Cs-oleate is a solid, so it was pre-heated to 100 °C before injection. $PbBr_2$ (225 mg 0.61 mmol), $ZnBr_2$ (552 mg, 2.45 mmol), ODE (15 mL) and oleylamine (6 mL) were evacuated in a 100-mL 3-neck flask at 100 °C. It was cooled to 70–80 °C, and then 0.3 mL of HBr (48 wt% in water) was swiftly injected under N_2. After 5 min, the solution was dried at 100 °C until $PbBr_2$ and $ZnBr_2$ salts had completely solubilized. OA (6 mL) was injected under N_2 and the

solution was dried for 10 min. The temperature was cooled to 80 °C under an N_2 atmosphere, and then 1.8 mL of Cs-oleate (prepared as described above) was quickly injected. The reaction was stopped by cooling in an ice-water bath after 3 min. The reacted solution was centrifuged with 45 mL of methyl acetate at 7,000 rpm for 1 min, then the supernatant was collected. After 115 mL of methyl acetate and 20 mL of hexane were added, the solution was centrifuged at 7,000 rpm for 1 min, then the supernatant was collected. Lastly, QDs were precipitated by adding 20 mL acetone and centrifuging at 7,000 rpm for 1 min, followed by dispersion in 15 mL of hexane. Precipitates were removed by centrifugation at 12000 rpm for 10 min. The resultant QDs were stored in hexane until subjected to ligand exchange.

Ligand Treatment of PeQDs: Benzoyl bromide (BnBr) and phenethyl amine (PEA) were diluted with toluene to a concentration of 1 µL mL^{-1}. QDs in 1 mL hexane (prepared as described above) were precipitated with ≈5 mL of methyl acetate by centrifugation at 10,000 rpm for 1 min. The precipitate was redispersed using 1 mL hexane and repeated 2 times more. During purification, the methyl acetate was added step-by-step (with 0.5–1 mL) and centrifuged when turbid, to remove unwanted products and obtain a narrow size distribution of QDs. For ligand exchange, the PeQD solution was mixed with certain amounts of pre-prepared BnBr solution and PEA solution (typically ≈200 µL ligand solution in 1 mL QD solution), and the PLQY increased directly. The QDs were obtained by centrifugation at 10,000 rpm for 5 min to precipitate them with additional methyl acetate, then dispersed in toluene

PeLED Fabrication and Characterization: First, 70-nm-thick ITO patterned glasses were cleaned by sequential sonication in acetone and isopropanol for 15 min each. The residual solvent was allowed to evaporate, then the ITO substrates were treated with ozone for 20 min. Then PEDOT:PSS was spin-coated to a layer thickness of 30 nm; the coated films were baked at 120 °C for 10 min, and then samples were transferred to an N_2-filled glove box fabrication of the HTL and PeQD film. For the HTL, Oxe-DCDPA dissolved 8 mg mL^{-1} in chlorobenzene was spin-coated and baked at 120 °C for 10 min to form a layer thickness of 15 nm. PeQD, or PeQD-mCP film was fabricated on the HTL. For PeQD-mCP film fabrication, the total concentration was adjusted to 5 mg mL^{-1}. Then the samples were moved to a high-vacuum evaporation chamber and a 45-nm-thick layer of CN-T2T, 1-nm-thick layer of LiF and a 100-nm-thick layer of Al were sequentially deposited as the cathode. The devices were encapsulated to maintain N_2 conditions and to exclude H_2O and O_2. A Keithley 236 device was used as a source measurement unit and a Minolta CS 2000 spectroradiometer was used to measure the luminance characteristics of the PeLEDs.

Characterization of PeQDs Solution: PL spectra were recorded using a JASCO FP8500 spectrofluorometer. To measure the PLQY of the PeQD solutions, the same spectrofluorometer was equipped with a 100-nm integrating sphere. PLQY values were calculated using Jasco SpectraManager II software. The absorbance of the PeQD solution was measured using UV–vis spectrometer (Lambda 465, PerkinElmer). Chemical analysis of PeQD surface was measured using attenuated total reflection (ATR) mode of FT-IR (Nicolet iS50, Thermo Fisher Scientific), and XPS (Versaprobe III, Ulvac-phi). UPS of the PeQD was measured using a photoelectron spectrometer (Axis Supra, Kratos). Top-view of the QD films was obtained using field-emission SEM (AURIGA, Carl Zeiss).

Transmission Electron Microscopy Measurement: Transmission electron microscopy images of PNCs were collected using a Themis-Z microscope operating at an acceleration voltage of 60 kV.

Transient EL Measurement: Transient EL was obtained using a system composed of a streak camera (C10627, Hamamatsu Photonics), a delay generator (DG645, Stanford Research Systems) and a function generator (Agilent 3250A). A voltage pulse with 5 ms width, 20 Hz repetition rate and the voltage around the turn-on voltage of the device (2.9 V) was used.

Transient PL Measurement: Transient PL decay and time-resolved spectra of the PeQD film were carried out with a system composed of a streak camera (C10627, Hamamatsu Photonics), a delay generator (DG645, Stanford Research Systems) and a nitrogen pulse laser (337 nm, Usho Optical systems).

Time-Correlated Single-Photon-Counting Measurement: PL lifetime was measured using a FluoTime 300 spectrometer. A picosecond-pulse laser head (LDH-P-C-405B, PicoQuant) was used to excite the samples at a laser wavelength of 405 nm. A photon-counting detector (PMA Hybrid 07) and time-correlated single-photon-counting module (PicoHarp, PicoQuant) were used to detect the PL decay and calculate the PL lifetimes of samples.

Optical Simulation: Optical simulations were performed using an optical simulation software package (J-OSTD, JooAm) based on the classical dipole model. The input parameters for the simulations including the refractive indices of the layers, and PL spectra of the EMLs are obtained from the experiments, and a fixed PLQY of 60% for both the QD-only and QD-mCP devices. Emitting dipole orientation was assumed to be isotropic.

Supporting Information

Supporting Information is available from the Wiley Online Library or from the author.

Acknowledgements

K.Y.J. and S.Y.H. contributed equally to this work. This work was supported by the National Research Foundation of Korea (NRF) grant funded by the Korea government (Ministry of Science, ICT & Future Planning) (NRF-2016R1A3B1908431, 2022M3H4A1A04096380). K.Y.J. acknowledges Korea Institute of Energy Technology Evaluation and Planning (KETEP) grant funded by the Korea government (MOTIE) (20214000000570, Fostering Next-generation Global Leader for Advanced Material Energy).

Conflict of Interest

Authors declare no conflict of interest.

Data Availability Statement

The data that support the findings of this study are available from the corresponding author upon reasonable request.

Keywords

deep-blue, electronic coupling, energy transfer, light-emitting diodes, perovskite quantum dots

Received: April 4, 2024
Revised: July 2, 2024
Published online:

[1] J. S. Kim, J.-M. Heo, G.-S. Park, S.-J. Woo, C. Cho, H. J. Yun, D.-H. Kim, J. Park, S.-C. Lee, S.-H. Park, E. Yoon, N. C. Greenham, T.-W. Lee, *Nature* **2022**, *611*, 688.
[2] J. I. Kim, Q. Zeng, S. Park, H. Lee, J. Park, T. Kim, T.-W. Lee, *Adv. Mater.* **2023**, *35*, 2209784.
[3] a) L. N. Quan, B. P. Rand, R. H. Friend, S. G. Mhaisalkar, T.-W. Lee, E. H. Sargent, *Chem. Rev.* **2019**, *119*, 7444; b) D.-H. Kim, S.-J. Woo, C. P. Huelmo, M.-H. Park, A. M. Schankler, Z. Dai, J.-M. Heo, S. Kim, G. Reuveni, S. Kang, J. S. Kim, H. J. Yun, J. Park, J. Park, O. Yaffe, A. M. Rappe, T.-W. Lee, *Nat. Commun.* **2024**, *15*, 6245.
[4] H. Cho, S.-H. Jeong, M.-H. Park, Y.-H. Kim, C. Wolf, C. L. Lee, J. H. Heo, A. Sadhanala, N. Myoung, S. Yoo, S. H. Im, R. H. Friend, T.-W. Lee, *Science* **2015**, *350*, 1222.

[5] T.-H. Han, K. Y. Jang, Y. Dong, R. H. Friend, E. H. Sargent, T.-W. Lee, *Nat. Rev. Mater.* **2022**, *7*, 757.
[6] Y. Chen, S. Lu, M. Nan, J. Xie, W. Shen, A. N. Aleshin, G. Cheng, S. Chen, W. Huang, *Adv. Opt. Mater.* **2023**, *11*, 2300473.
[7] Q. Wang, X. Wang, Z. Yang, N. Zhou, Y. Deng, J. Zhao, X. Xiao, P. Rudd, A. Moran, Y. Yan, J. Huang, *Nat. Commun.* **2019**, *10*, 5633.
[8] M. Karlsson, Z. Yi, S. Reichert, X. Luo, W. Lin, Z. Zhang, C. Bao, R. Zhang, S. Bai, G. Zheng, P. Teng, L. Duan, Y. Lu, K. Zheng, T. Pullerits, C. Deibel, W. Xu, R. Friend, F. Gao, *Nat. Commun.* **2021**, *12*, 361.
[9] J. Yao, L. Wang, K. Wang, Y. Yin, J. Yang, Q. Zhang, H. Yao, *Kexue Tongbao (Foreign Lang. Ed.)* **2020**, *65*, 1150.
[10] F. Zhang, J. Song, B. Cai, X. Chen, C. Wei, T. Fang, H. Zeng, *Kexue Tongbao (Foreign Lang. Ed.)* **2021**, *66*, 2189.
[11] F. Chun, K. Y. Jang, T.-W. Lee, *Kexue Tongbao (Foreign Lang. Ed.)* **2021**, *66*, 2159.
[12] Y. Dong, Y. K. Wang, F. Yuan, A. Johnston, Y. Liu, D. Ma, M. J. Choi, B. Chen, M. Chekini, S. W. Baek, L. K. Sagar, J. Fan, Y. Hou, M. Wu, S. Lee, B. Sun, S. Hoogland, R. Quintero-Bermudez, H. Ebe, P. Todorovic, F. Dinic, P. Li, H. T. Kung, M. I. Saidaminov, E. Kumacheva, E. Spiecker, L. S. Liao, O. Voznyy, Z. H. Lu, E. H. Sargent, *Nat. Nanotechnol.* **2020**, *15*, 668.
[13] C. Bi, Z. Yao, X. Sun, X. Wei, J. Wang, J. Tian, *Adv. Mater.* **2021**, *33*, 2006722.
[14] F. Chun, K. Y. Jang, H. Zhou, S. Kim, E. Yoon, T.-W. Lee, *Small* **2024**, 2400959.
[15] Y. Jiang, C. Sun, J. Xu, S. Li, M. Cui, X. Fu, Y. Liu, Y. Liu, H. Wan, K. Wei, T. Zhou, W. Zhang, Y. Yang, J. Yang, C. Qin, S. Gao, J. Pan, Y. Liu, S. Hoogland, E. H. Sargent, J. Chen, M. Yuan, *Nature* **2022**, *612*, 679.
[16] F. Zhang, C. Xiao, Y. Li, X. Zhang, J. Tang, S. Chang, Q. Pei, H. Zhong, *Front Chem* **2018**, *6*, 444
[17] C. Bi, Z. Yao, J. Hu, X. Wang, M. Zhang, S. Tian, A. Liu, Y. Lu, N. H. de Leeuw, M. Sui, J. Tian, *ACS Energy Lett.* **2023**, *8*, 731.
[18] Y. Tong, E. -P. Yao, A. Manzi, E. Bladt, K. Wang, M. Döblinger, S. Bals, P. Müller-Buschbaum, A. S. Urban, L. Polavarapu, J. Feldmann, *Adv Mater* **2018**, *30*, 1801117.
[19] R. Koole, P. Liljeroth, C. de Mello Donegá, D. Vanmaekelbergh, A. Meijerink, *J. Am. Chem. Soc.* **2006**, *128*, 10436.
[20] A. Zabet-Khosousi, A. A. Dhirani, *Chem. Rev.* **2008**, *108*, 4072.
[21] T. Hanrath, *J. Vac. Sci. Techno. A* **2012**, *30*, 030802.
[22] G. M. Akselrod, F. Prins, L. V. Poulikakos, E. M. Y. Lee, M. C. Weidman, A. J. Mork, A. P. Willard, V. Bulović, W. A. Tisdale, *Nano Lett.* **2014**, *14*, 3556.
[23] A. J. Mork, M. C. Weidman, F. Prins, W. A. Tisdale, *J. Phys. Chem. C* **2014**, *118*, 13920.
[24] R. H. Gilmore, E. M. Y. Lee, M. C. Weidman, A. P. Willard, W. A. Tisdale, *Nano Lett.* **2017**, *17*, 893.
[25] K. F. Chou, A. M. Dennis, *Sensors (Switzerland)* **2015**, *15*, 13288.
[26] X. Tang, D. Rossi, J. Cheon, D. H. Son, *Chem. Mater.* **2022**, *34*, 7181.
[27] O. I. Mićić, S. P. Ahrenkiel, A. J. Nozik, *Appl. Phys. Lett.* **2001**, *78*, 4022.
[28] H. M. Jang, S. H. Lee, K. Y. Jang, J. Park, T.-W. Lee, *Commun. Phys.* **2023**, *6*, 372.
[29] K.-W. Tsai, M.- K. Hung, Y.-H. Mao, S.-A. Chen, *Adv. Funct. Mater.* **2019**, *29*, 1901025.
[30] H. Pashaei Adl, S. Gorji, G. Muñoz-Matutano, R. I. Sánchez-Alarcón, R. Abargues, A. F. Gualdrón-Reyes, I. Mora-Seró, J. P. Martínez-Pastor, *J Lumin* **2021**, *240*, 118453.
[31] C. Zhu, L. G. Feld, M. Svyrydenko, I. Cherniukh, D. N. Dirin, M. I. Bodnarchuk, V. Wood, N. Yazdani, S. C. Boehme, M. V. Kovalenko, G. Rainò, *Adv. Opt. Mater.* **2024**, *12*, 2301534.
[32] W.-Y. Hung, P. Y. Chiang, S.-W. Lin, W.-C. Tang, Y.-T. Chen, S.-H. Liu, P.-T. Chou, Y. T. Hung, K.-T. Wong, *ACS Appl. Mater. Interfaces* **2016**, *8*, 4811.
[33] C.-H. Hsiao, S.-W. Liu, C.-T. Chen, J.-H. Lee, *Org. Electron.* **2010**, *11*, 1500.
[34] H. Shin, S. Lee, K. H. Kim, C. K. Moon, S. J. Yoo, J. H. Lee, J. J. Kim, *Adv. Mater.* **2014**, *26*, 4730.
[35] Y. Cao, N. Wang, H. Tian, J. Guo, Y. Wei, H. Chen, Y. Miao, W. Zou, K. Pan, Y. He, H. Cao, Y. Ke, M. Xu, Y. Wang, M. Yang, K. Du, Z. Fu, D. Kong, D. Dai, Y. Jin, G. Li, H. Li, Q. Peng, J. Wang, W. Huang, *Nature* **2018**, *562*, 249.
[36] B. Zhao, M. Vasilopoulou, A. Fakharuddin, F. Gao, A. R. M. Yusoff, R. H. Friend, D. Di, *Nat. Nanotechnol.* **2023**, *18*, 981.
[37] R. Liu, Z. Gan, R. Shinar, J. Shinar, *Phys Rev B Condens Matter* **2011**, *83*, 245302.
[38] J. H. Lee, S. Lee, S. J. Yoo, K. H. Kim, J. J. Kim, *Adv. Funct. Mater.* **2014**, *24*, 4681.
[39] C. Pu, X. Dai, Y. Shu, M. Zhu, Y. Deng, Y. Jin, X. Peng, *Nat. Commun.* **2020**, *11*, 937.
[40] J. He, Z. Liu, Z. Cao, H. Zhang, Y. Meng, B. Chen, D. Zhong, *J. Phys. Chem. Lett.* **2020**, *11*, 2550.